Topographic Analysis of Two-Wavelength Autofluorescence Supports Higher Macular Xanthophyll Pigment in AMD Than Aging: ALSTAR2 Baseline

Lukas Goerdt,[1,2] Andreas Berlin,[1,3] Liyan Gao,[1] Thomas A. Swain,[1] Sarah S. Kim,[1] Gerald McGwin,[1] Mark E. Clark,[1] Deepayan Kar,[1] Cynthia Owsley,[1] Kenneth R. Sloan,[1] and Christine A. Curcio[1]

[1]Department of Ophthalmology and Visual Sciences, Heersink School of Medicine, University of Alabama at Birmingham, Birmingham, Alabama, United States
[2]Department of Ophthalmology, University of Bonn, Bonn, Germany
[3]Department of Ophthalmology, University of Würzburg, Würzburg, Germany

PURPOSE. To advance metabolic imaging of the high-risk macula lutea by quantifying the topography of macular pigment optical density (MPOD), measured with two-wavelength autofluorescence (2WAF), and quantitative (short-wavelength) autofluorescence (qAF) intensity, which share the same signal source and cross-retinal light path, in aging, early (e), and intermediate (i) age-related macular degeneration (AMD).

METHODS. 2WAF and qAF images of 384 pseudophakic eyes of 230 persons (mean age, 74.2 ± 5.7 years; 145 female) from ALSTAR2 (AREDS 9-step classification: 170, normal; 118, eAMD; 96 iAMD) were shown as maps (intensity, z-score) and meridian plots. Correlations were determined in Early Treatment Diabetic Retinopathy Study (ETDRS) subfields.

RESULTS. MPOD was higher in the central subfield ($P < 0.01$) in iAMD compared to eAMD and normal eyes, and qAF was lower in the central subfield and inner ring (both $P < 0.01$) in AMD compared to normal eyes. MPOD differed along horizontal versus vertical meridians, depending on disease stage. Pixel-level z-score maps and meridian plots showed distinct annuli of alternating levels of MPOD anchored on the foveal center, unrelated to qAF. Across the central subfield, high 2WAF was associated with low qAF in all disease stages ($r = -0.47$, $r = -0.47$, $r = -0.42$; all $P < 0.001$). In the inner ring, correlations were significant for normal and eAMD only ($r = -0.31$, $P = 0.004$ and $r = -0.22$, $P \leq 0.001$, respectively).

CONCLUSIONS. New analytics support previously reported higher MPOD in AMD compared to normal eyes, especially central subfield and inner ring. MPOD and qAF differ by disease-stage–related topography and correlations, supporting independent use in metabolic imaging of the macula lutea.

Keywords: age-related macular degeneration, fundus autofluorescence, xanthophyll carotenoids, pixel arithmetic, fovea, Müller glia, retinal pigment epithelium

Age-related macular degeneration (AMD) causes central blindness in older adults worldwide.[1] Currently approved treatments target exudative and atrophic end stages.[2–4] Approaches to earlier disease stages are avidly sought. One safe, efficacious, and cost-effective intervention is oral supplementation with antioxidants.[5–7] These include two polar xanthophyll carotenoids of dietary origin, lutein and zeaxanthin, plus an intraocularly synthesized metabolite, meso-zeaxanthin. Together, these comprise the macular pigment (MP) and impart a characteristic yellow hue (macula lutea).

The xanthophyll bioavailability axis from foods to target tissue includes digestion, absorption, transport, and uptake by and stabilization within retinal cells.[8–11] Two-wavelength autofluorescence (2WAF) imaging reveals retinal xanthophyll in vivo, one aspect of bioavailability. This technique uses strong emissions elicited from retinal pigment epithelium (RPE) organelles (lipofuscin and melanolipofuscin) by blue and green excitation lights (488-nm and 514-nm wavelengths, respectively) (Fig. 1).[12] Xanthophyll carotenoids absorb blue but not green light. MP optical density (MPOD) is the $\log_{10}$ ratio of green emissions to blue emissions at specific regions of interest, compared to a reference point where MPOD is near zero.[12,13] Relative to psychophysical tests involving color matching at selected locations in visual space,[14] 2WAF imaging is quick, objective, repeatable, and comprehensive (i.e., all pixels are analyzable).
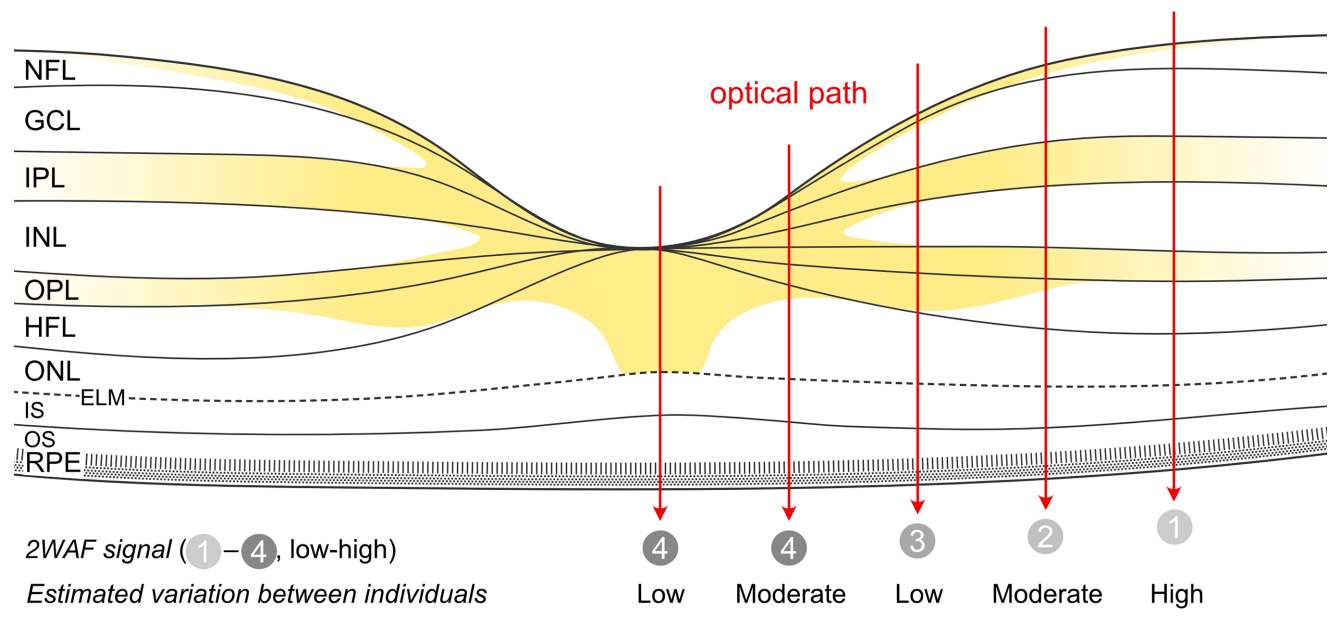
FIGURE 1. Distribution of xanthophyll carotenoids and incoming light path in macula lutea. The *yellow areas* show the distribution of macular xanthophyll carotenoids within the macula lutea (−3 mm diameter, indicated by the bar at the bottom, ETDRS central subfield, and inner ring). Tissue-level laboratory studies previously visualized this distribution,[71,97,98] which follows the distribution of cells around the foveal center, particularly Müller glia and photoreceptors. The layer of RPE cell bodies is depicted with melanosomes in apical processes and lipofuscin and melanolipofuscin in the cell body, as shown by volume electron microscopy. Lipofuscin and melanolipofuscin are the major signal sources for short-wavelength autofluorescence imaging. *Red arrows* show the path of incoming light. Numbers indicate the measured macular pigment optical density signal in two-wavelength autofluorescence. Variation between individuals (numbers along bottom) is shown qualitatively for discussion purposes. The 2WAF signal at the camera decreases in a radial fashion with distance from the foveal center, herein defined as the inward rise of the external limiting membrane. Variation in signal between individual eyes depends on xanthophyll concentrations in retinal layers and layer thicknesses. Choriocapillaris and choroid are not shown. ELM, external limiting membrane; GCL, ganglion cell layer; HFL, Henle fiber layer; INL, inner nuclear layer; IPL, inner plexiform layer; IS, inner segment; NFL, nerve fiber layer; ONL, outer nuclear layer; OPL, outer plexiform layer; OS, outer segment. Modified from figure 5 in Kar et al.[23]

New data about foveal biology and metabolic imaging technologies for foveal cells, such as 2WAF, could help elucidate why AMD predilection is so spatially focal on the retina. This information in turn can be used to enhance layer-by-layer imaging by optical coherence tomography (OCT), currently the dominant technology for most outer retinal disease diagnosis and management. Recent reanalysis of color fundus photography–based epidemiology and trial data showed the risk for AMD onset and early progression to be extraordinarily concentrated within the macula lutea.[15–17] Further, risk is threefold higher in the 1-mm-diameter central subfield of the Early Treatment of Diabetic Retinopathy Study (ETDRS) grid, where foveal cones are abundant and rods nearly absent, than in the inner ring. In fact, the spatial distribution of the risk profile matches that of macular xanthophylls as determined by 2WAF imaging, rather than that of cone photoreceptors.[18]

The Alabama Study on Early Age-Related Macular Degeneration 2 (ALSTAR2) longitudinally studies retinal structure and visual function during the transition from aging to AMD.[19,20] The underlying hypothesis is a center-surround model of cone resilience and rod vulnerability united with deposit-driven AMD progression in the macula lutea.[15,19] ALSTAR2 2WAF studies showed more retinal MPOD integrated over the ETDRS grid in AMD eyes than in healthy aged controls,[21] as well as higher serum levels of xanthophylls. These effects could not be attributed to supplement use[21] and align with other reports also using 2WAF imaging.[22,23] These data challenge the idea that AMD retinas

are deficient in xanthophylls, the rationale for oral supplementation strategies. As shown in Figure 1, 2WAF shares a signal source and a light path across the retina with short-wavelength fundus autofluorescence and thus variation should be interpreted considering the latter from the same eyes. In ALSTAR2 participants, quantitative autofluorescence (qAF)[24] intensity assessed with novel metrics decreased with AMD severity in the macula lutea and could thus contribute to the increase in 2WAF signal.

The present study using ALSTAR2 baseline data had two goals. First, we described the topography of the 2WAF signal in aged and AMD eyes to localize the high MPOD signal in AMD. Second, we compared 2WAF and qAF imaging in the same eyes using *z*-score maps, meridian plots, and correlation statistics to investigate the interdependence of these two metabolic imaging techniques.

METHODS

Patient Selection

Participants ≥60 years old were selected from the comprehensive ophthalmology clinic of the Callahan Eye Hospital Clinic of the Department of Ophthalmology and Visual Sciences at the University of Alabama at Birmingham for ALSTAR 2 participation as previously described.[19] In brief, AMD patients were identified using electronic medical records reviewed (by author CO) and screened for confounding ocular and systemic diseases (refer to the Supplementary

Materials for details). Pseudophakic eyes with high-quality retinal imaging from the baseline cohort were selected to avoid the impact of the natural lens on autofluorescence imaging.[25–27]

AMD status was determined by color fundus photographs (450+; Carl Zeiss Meditec, Jena, Germany) according to the Age-Related Eye Disease Studies (AREDS) nine-step classification system[28] by one experienced grader (author MEC). The AREDS classification has a strong epidemiological basis using a classification and regression tree analysis[29] and was used for a power analysis in the initial design of ALSTAR2.[19,28] Intra-reader reliability ($\kappa = 0.88$) and inter-reader reliability ($\kappa = 0.75$) for this approach are good.[30]

Image Acquisition

After pupil dilation using 1% tropicamide and 2.5% phenylephrine hydrochloride eye drops, participants underwent multimodal retinal imaging, including OCT (horizontally oriented, centered on the fovea; scan field, 30° × 25°; 121 B-scans; interscan distance, 60 μm; automatic real time averaging > 9), 2WAF, qAF (all on SPECTRALIS HRA+OCT, Heidelberg Engineering, Heidelberg, Germany), and color fundus photography (Zeiss 450+).[19]

The investigational MPOD module for the SPECTRALIS uses confocal scanning laser ophthalmoscopy with blue and green diodes for excitation (wavelengths of 488 and 514 nm, respectively) in a 30° × 30° scan field (768 × 768 pixels), centered on the fixation point. This technique provides excellent repeatability.[31] Images that were unevenly illuminated, poorly focused, or partially shadowed by vitreous opacities were excluded (author AB).[21]

The SPECTRALIS also contains an internal qAF reference (excitation, 488 nm; emission, 500–750 nm) that is excited simultaneously with the fundus over the same field of view as the MPOD module. A scaling factor (in retinal micrometers per pixel) using individual participants' corneal c-curves and the focus setting of the SPECTRALIS was used to adjust images for variations among subjects. This factor was standardized by the manufacturer's software based on the scaling factor of an emmetropic eye with a corneal curvature of 7.7 mm.[24,32] Autofluorescence intensity is attenuated at the camera by photopigments in photoreceptors that absorb incoming light and prevent it from reaching RPE fluorophores. Therefore, photoreceptors were bleached for 20 seconds before image acquisition to minimize this effect. Twelve single qAF grayscale images were registered per eye and checked for homogeneous illumination and foveal centration.[33–35] Images with artifacts were removed, and eyes with fewer than nine qualifying images were disregarded. Qualifying images were used to create an average grayscale qAF image using the manufacturer's software. This approach was previously assessed for repeatability in inter-session and interday testing, providing high repeatability (intraclass correlation coefficient, 0.91–0.96) and moderate repeatability (intraclass correlation coefficient, 0.77).[33,36–38]

Image Processing

The 2WAF and qAF images were exported to ImageJ (National Institutes of Health, Bethesda, MD, USA) for post-processing.[39] All plug-ins used for this study are available from the ImageJ update site at https://sites.imagej.net/CreativeComputation/ and are summarized in chronological order in Supplementary Table S1. MPOD values were calculated from 2WAF images and normalized by setting the mean MPOD value at 9° eccentricity[40] to 0 (plug-in: MPOD XML Reader). To plot MPOD values along cardinal meridians and investigate radial symmetry (Figs. 2, 3), MPOD was averaged within four (two per meridian) 30° wedges with tips at the fovea (plug-in: Grids OCT). For reference, the SPECTRALIS software plots one average meridian, assuming radial symmetry.[41] qAF values were calculated using a custom tool (plug-in: QAF XML Reader) as described previously.[24,42,43]

Map Creation

To visualize MPOD and qAF topography as maps, we created stacks of all images of one modality, including all eyes of one disease group (plug-in: Batch_Standard_Retina). The foveal center and the closest edge of the optic nerve head served as references. The foveal center was defined as the highest elevation of the external limiting membrane at a central bouquet formed by the longest cones and interleaved Müller glia.[44,45] To create a mean intensity value for each pixel, the sum of intensities at every pixel was divided by the number of images per stack. These were created separately for AREDS normal, early AMD (eAMD), and intermediate AMD (iAMD) eyes (plug-in: Math).

The macula lutea is characterized by high interindividual variability in cone density, retinal thickness, and pit morphology due to multilayer cellular repositioning during development.[46] This variability factored into a decision to not include the macula lutea in the qAF8 metric (eight segments in an annulus; 6.0°–8.1° inner–outer radius).[33] In our recent publication on qAF in ALSTAR2, we explored variability using a new pixel-level analytic outcome (z-score maps).[24] For each pixel of each eye, the difference between the value of the observation and the mean of all eyes was divided by the standard deviation of all eyes at that pixel (plug-in: Compare_SD). In maps, intensities at each pixel were expressed as z-score units and color-coded to indicate ± 0.5 SD above or below the mean at that pixel. This revealed for the first time progressively lower qAF signal in aging, eAMD, and iAMD eyes across the macula lutea.[24,35]

Herein we used the same method to compare 2WAF and qAF datasets, which are generated with different units of measurement. Data from the standard retinas were converted into z-scores (Fig. 4). Following a publicly available protocol (https://imagej.net/ij/plugins/lut-editor.html), a custom color scale was produced and applied to the maps. In addition, cutouts of the central ETDRS subfield plus inner ring were enlarged to highlight features in the fovea where photoreceptors and RPE cells are small and cross-layer effects may be visible (Fig. 1).

Statistical Analysis

Demographics, visual acuity, and AMD status were summarized using means and standard deviations or number and percent for continuous and categorical data, respectively. MPOD and qAF values were averaged within the central ETDRS subfield (diameter, 1 mm), inner ring (inner–outer diameter, 1–3 mm), and outer ring (inner–outer diameter, 3–6 mm).[15] Generalized estimating equations were used to compare MPOD, qAF, and visual acuity between disease groups. All comparisons were adjusted for the nested data structure of two eyes within one patient where applicable. These averages were used to calculate Pearson's correlation
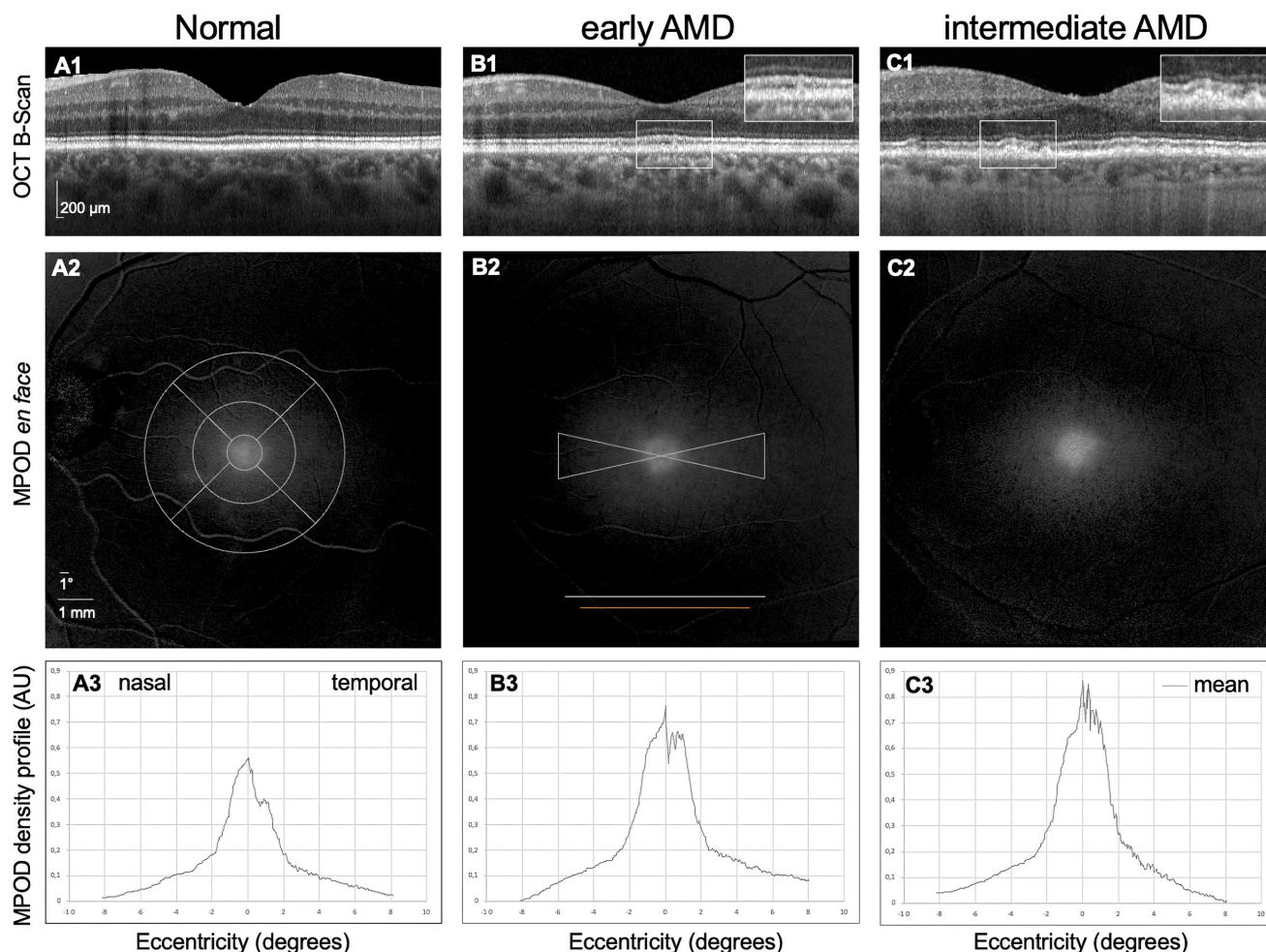
FIGURE 2. MPOD distribution of one exemplary case per disease group. (**A1–A3**) Left eye of a 79-year-old female patient, including foveal OCT B-scan, MPOD en face image, and MPOD density profile. AREDS nine-step stage 1 (normal). (**B1–B3**) Left eye of a 73-year-old male patient. AREDS nine-step stage 4 (early AMD). (**C1–C3**) Left eye of a 76-year-old male patient. AREDS nine-step stage 6 (intermediate AMD). *Insets* in **B1** and **C1** show OCT alterations relevant for AREDS nine-step classification. The *white line* in **B2** shows where MPOD was assessed for **A3** to **C3**. The *orange line* in **B2** describes the extent of the B-scan displayed in **A1** to **C1**. The bow-tie–like structure in **B2** shows the area from which MPOD values were averaged. (**A3–C3**) Mean MPOD profiles, with 11 values at equally distributed eccentricities taken from wedges with tips at the foveal center and 30° width at the nasal and temporal extremities. An increase of MPOD from normal to eAMD to iAMD is apparent.

coefficients for each ETDRS region and disease group. $P < 0.05$ was considered statistically significant. This analysis employed SAS 9.4 (SAS Institute, Cary, NC, USA). The results shown in Figure 5 were plotted using R (ggplot2 package; R Foundation for Statistical Computing, Vienna Austria).[47,48] Although the distance from the foveal center (eccentricity) was a much larger effect in the photoreceptor distribution (~33-fold) than the angle around the fovea (meridian), the maps described above guided us to also compare qAF and MPOD values in all ETDRS subfields. Means, standard errors, and z-scores for MPOD and qAF along the horizontal and vertical meridians were calculated and plotted using MATLAB 9.5 (MathWorks, Natick, MA, USA).

RESULTS

Cohort Characteristics

Table 1 summarizes patient-level characteristics of the study sample. A total of 384 eyes of 230 participants (145 female;

mean age, 74.1 ± 5.7 years) were included. Table 2 summarizes eye-level characteristics. Of these, 170 eyes were classified as AREDS normal, 118 as eAMD, and 96 as iAMD. Best-corrected visual acuity was better in normal and eAMD eyes compared to iAMD eyes (0.02 ± 0.13 logMAR vs. 0.02 ± 0.14 logMAR vs. 0.07 ± 0.13 logMAR; $P = 0.02$).

MPOD and qAF Distribution Across Disease Groups

Figure 2 shows 2WAF images and MPOD values along the horizontal meridian through the foveal center in one exemplary eye of each AREDS diagnostic group. MPOD abundance peaked at or near the foveal center in every group and declined with increasing eccentricity. Table 2 shows significantly higher MPOD values in the central subfield ($P < 0.01$) but not in the inner ($P = 0.17$) and outer rings ($P = 0.70$) of iAMD and eAMD compared to normal eyes. Conversely, qAF values in the central subfield ($P < 0.01$) and inner
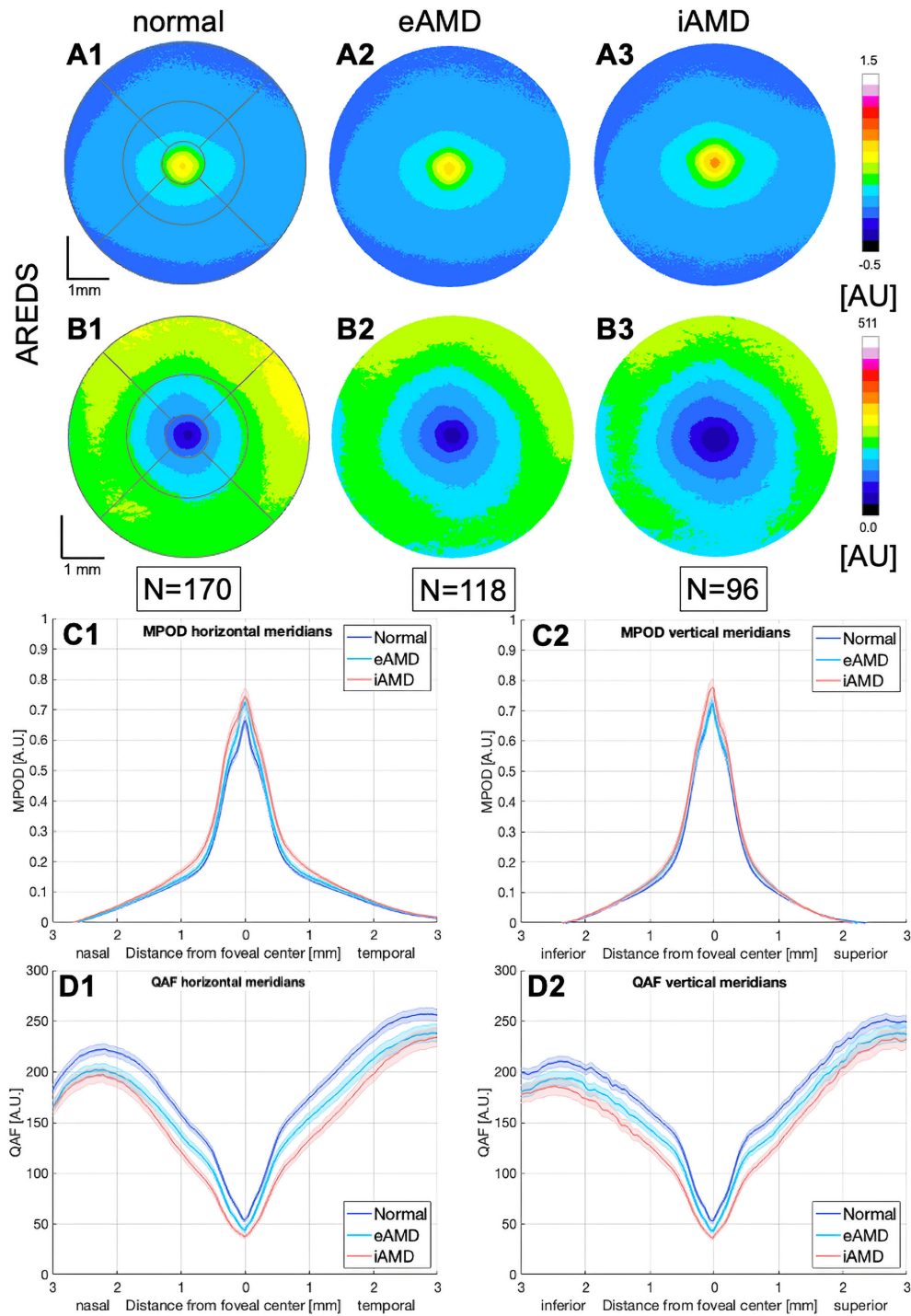
FIGURE 3. MPOD and qAF standard retinas for eyes stratified by AREDS. (**A1–A3**) Standard retinas for MPOD in normal, eAMD, and iAMD eyes. A gradual increase of MPOD from normal over eAMD to iAMD is visible, which is most present at the inner ETDRS ring. (**B1–B3**) Standard retinas for qAF in normal, eAMD, and iAMD eyes. A decline in qAF from normal over eAMD to iAMD is visible. This is most apparent in the central subfield and the inner ETDRS ring. (**A1, B1**) The ETDRS grid is overlaid. (**C1, C2**) Horizontal and vertical meridian plots for MPOD. *Shaded bands* indicate the standard error. MPOD is higher in iAMD compared to eAMD and normal eyes, particularly in the foveal center and 0.5- to 1.0-mm eccentricity nasal and temporal. (**D1, D2**) Horizontal and vertical meridian plots for qAF. *Shaded bands* indicate the standard error. qAF is lower in iAMD compared to eAMD and normal eyes, differing by a similar absolute amount between stages.
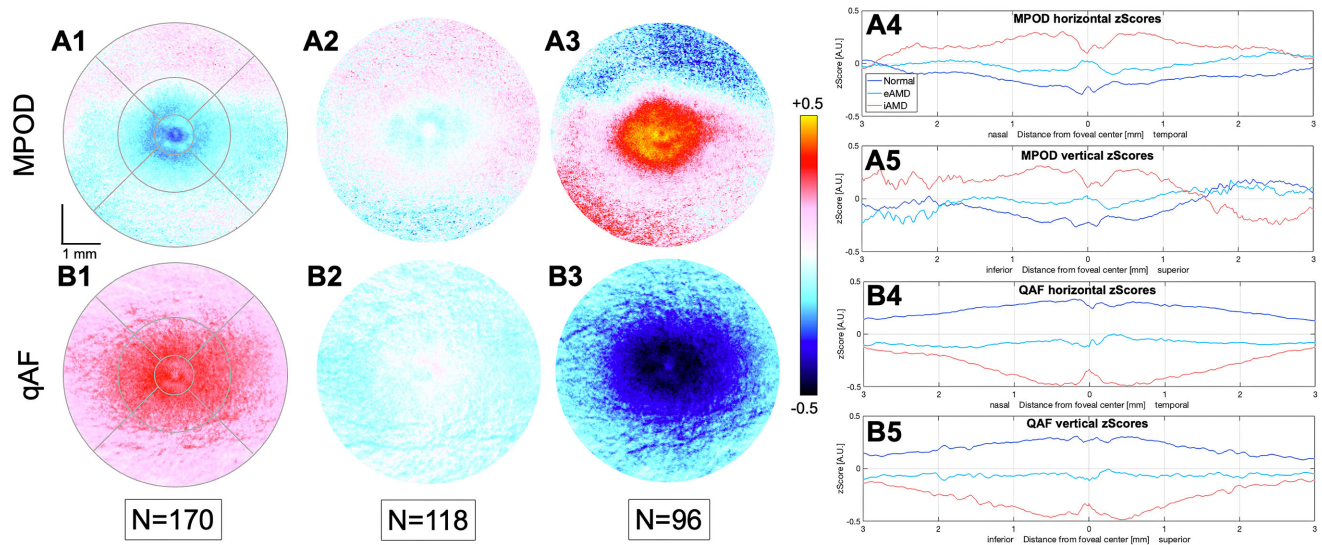
FIGURE 4. MPOD and qAF *z*-score maps for AREDS stratified aged and AMD eyes. (**A1–A3**) *z*-Score maps for MPOD in normal, eAMD, and iAMD eyes, with ETDRS grid shown in **A1**. An increase in MPOD is perceivable from normal over eAMD to iAMD eyes. Superior to the fovea, iAMD eyes show below-average MPOD values. (**A4**) MPOD *z*-scores along the horizontal meridian. (**A5**) MPOD *z*-scores along the vertical meridian. The difference between superior and inferior retina from **A3** is confirmed by the plots. (**B1–B3**) The *z*-scores for qAF in normal, eAMD, and iAMD eyes, with ETDRS grid shown in **B1**. In contrast to MPOD, qAF values decrease in later disease stages. No difference between superior and inferior retina was noted. (**B4**) qAF *z*-scores along the horizontal meridian. (**B5**) qAF *z*-scores along the vertical meridian.
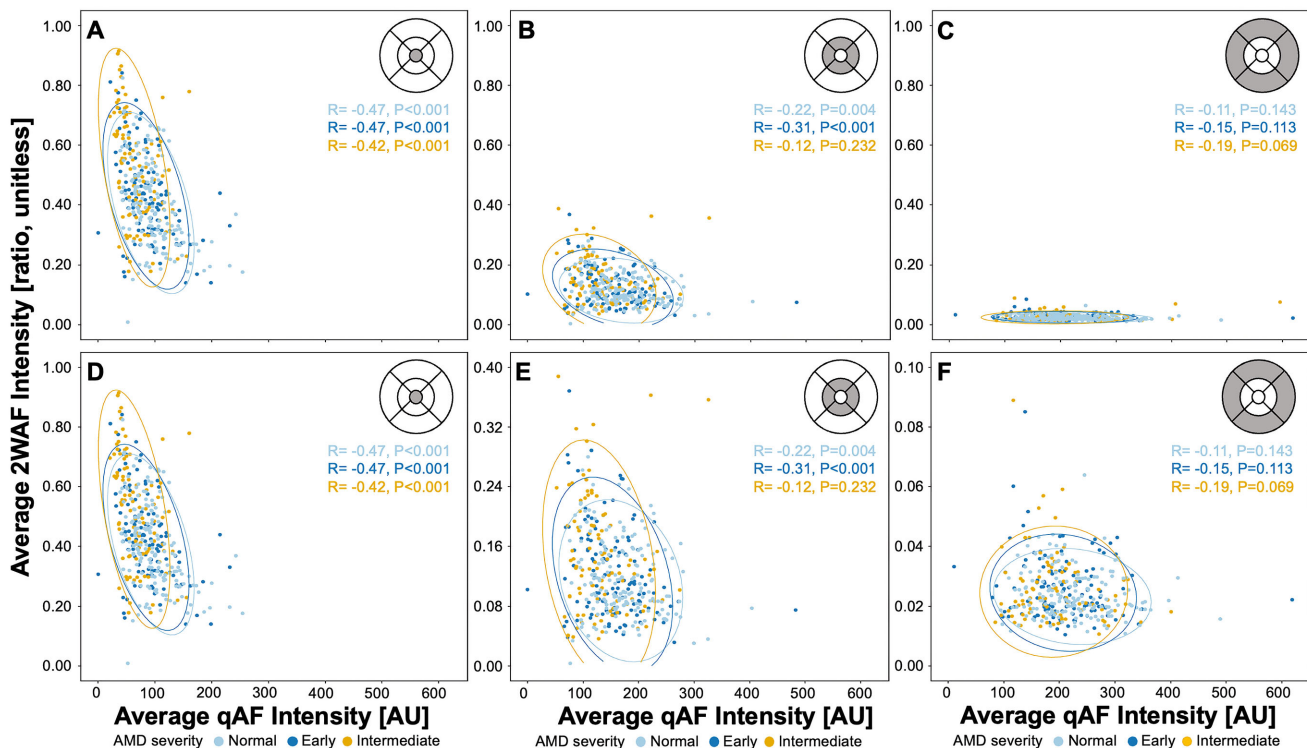

FIGURE 5. Comparison of mean 2WAF and qAF intensities for each AREDS disease stage in ETDRS rings. (**A–C**) The *x*-axes are scaled identically to show all data points. (**D–F**) The *x*-axes are scaled to the maximal *x* at each disease stage to show individual data points. (**A, D**) Average 2WAF values (ratio ranging from 0.00–1.00, no unit) of the central ETDRS subfield are plotted against average qAF values (−25 to 650 to accommodate all data points, *grayscale* [AU]), separated by disease staging according to the AREDS grading system. The ellipses show the 95% confidence intervals. Significant correlations of different magnitudes were found for all disease stages. (**B, E**) Average 2WAF and qAF values of the inner ETDRS ring. Significant correlations were found for normal and early AMD eyes. In **B**, values are crowded at the lower end of the scale. (**C, F**) No significant correlations were found for any disease stage in the outer ETDRS ring. 2WAF values were near zero, as shown in **C**.

TABLE 1. Cohort Characteristics.

Characteristic	Value
Patients, *n*	230
Eyes, *n*	384
Age (y), mean $\pm$ SD	74.2 $\pm$ 5.7
Female, *n* (%)	145 (63.0)
Ethnicity, *n* (%)	
Non-Hispanic	230 (100)
White	214 (93.0)
African American	13 (5.7)
Pacific Islander	2 (0.9)
American Indian	1 (0.4)
Smoking, *n* (%)	109 (47.7)
Oral carotenoid supplements, *n* (%)	62 (27.0)

($P < 0.01$) and outer rings ($P = 0.04$) were lower in iAMD and eAMD eyes compared to normal eyes.

Topographical Representation of MPOD and qAF

Figures 3A1 to 3A3 show maps of MPOD topography within the ETDRS grid of 384 eyes. The standard retinas for each diagnostic group show high MPOD at the foveal center, which declines with greater eccentricity in all directions. Of note, the central area of high MPOD (orange colors in Fig. 3) was enlarged in more advanced disease stages. Figure 3C1 and 3C2 display MPOD values along the horizontal and vertical meridians. Close examination of these plots reveals higher peak MPOD values for iAMD compared to eAMD and normal eyes at the foveal center. Meridional differences appeared in the parafovea (i.e., higher MPOD values in iAMD than in eAMD and normal on the horizontal meridian), whereas no such difference was apparent on the vertical meridian. Disease-related changes in MPOD distribution hence were not radially symmetrical.

Figures 3B1 to 3B3 show qAF standard retina maps for the ETDRS grid of all 384 eyes. qAF was low within the central subfield and smoothly higher toward the ETDRS margin with greater severity, more so in the outer superior and temporal subfields. The meridian plots in Figures 3D1 and 3D2 demonstrate this smooth increase. The meridian plots also show that the differences in qAF intensity were similar in magnitude among AMD stages, across eccentricities, and between meridians.

z-Score Maps for MPOD and qAF

Figures 4A1 to 4A3 show *z*-score maps of MPOD. Blue indicates that the mean MPOD value at that pixel was below the

mean of all study eyes at that pixel, white indicates pixels close to the mean, and red/yellow indicate above the mean. The maps show that, relative to normal eyes, MPOD was markedly higher within the central subfield and inner ring of iAMD, consistent with the meridian plots of Figure 3. Annuli of varying MPOD within the central subfield and inner ring appeared in both normal and AMD eyes, as expected from the model of Figure 1. The annuli are highlighted at higher magnification in Supplementary Figure S1. Unexpectedly, overall lower MPOD values in the superior outer ring and higher values in the inferior outer ring at iAMD had no equivalent nasally and temporally. These differences are clear in the *z*-score meridian plots (Fig. 4A4 and Fig. 5), where values for the vertical meridian cross each other in eAMD and iAMD eyes and values for the horizontal meridian remain separate.

Figures 4B1 to 4B5 show *z*-score maps and meridian plots for qAF. In stark contrast to the MPOD *z*-score maps, the qAF *z*-score maps are relatively even in intensity across the central subfield and inner ring in all disease groups. Accordingly, the meridian plots of the disease groups are separated widely and evenly across the entire central area. At higher magnification (Supplementary Fig. S1), some detail is discernible in the central subfield of qAF (i.e., some hint of the annuli seen in MPOD and a tiny bump at the foveal center in normal and iAMD eyes). The *z*-score difference maps of eAMD and iAMD eyes compared to normal eyes (Supplementary Fig. S2) reveal a much smaller area of higher MPOD compared to lower qAF. In summary, the area of increased MPOD centrally in iAMD eyes cannot be attributed to a decrease in qAF in the same retinal locations.

Correlation Analysis

Correlation coefficients between qAF and 2WAF values were calculated for each diagnostic group in rings of the ETDRS grid (Fig. 5). In the central ETDRS subfield, high 2WAF was significantly associated with low qAF for normal, eAMD, and iAMD eyes (all $P < 0.0001$) (Figs. 5A, 5D). The correlation was stronger ($r = -0.47$) in normal and eAMD eyes compared to iAMD eyes (both $r = -0.42$). In the inner ring (Figs. 5B, 5E), correlations followed the same direction and were significant for normal and eAMD eyes ($P = 0.004$ and $P = 0.001$, respectively) but not for iAMD eyes ($P = 0.232$). Interestingly, the correlation was stronger in eAMD eyes ($r = -0.31$) compared to normal eyes ($r = -0.22$). The outer ring lacked significant correlations for all disease groups (normal, $P = 0.143$; eAMD, $P = 0.111$; iAMD, $P = 0.069$) (Figs. 5C, 5F). For completeness due to the meridional differences between MPOD and qAF described above, Supplementary Figure S3

TABLE 2. Eye-Level Descriptors in Eyes Stratified by AREDS Nine-Step Classification

	All Eyes	Normal	eAMD	iAMD	*P*
N	384	170	118	96	**<0.01**
BCVA (logMAR), mean $\pm$ SD	0.03 $\pm$ 0.13	0.02 $\pm$ 0.13	0.02 $\pm$ 0.14	0.07 $\pm$ 0.13	**0.02**
MPOD, mean $\pm$ SD					
Central subfield	0.44 $\pm$ 0.16	0.40 $\pm$ 0.14	0.43 $\pm$ 0.15	0.52 $\pm$ 0.18	**<0.01**
Inner ring	0.13 $\pm$ 0.06	0.12 $\pm$ 0.05	0.13 $\pm$ 0.06	0.15 $\pm$ 0.08	0.14
Outer ring	0.03 $\pm$ 0.01	0.02 $\pm$ 0.01	0.03 $\pm$ 0.01	0.03 $\pm$ 0.01	0.70
qAF (AU), mean $\pm$ SD					
Central subfield	85.8 $\pm$ 38.6	96.3 $\pm$ 38.6	86.1 $\pm$ 39.1	66.7 $\pm$ 30.3	**<0.01**
Inner ring	155.6 $\pm$ 56.2	169.5 $\pm$ 53.9	153.7 $\pm$ 57.7	133.4 $\pm$ 51.0	**<0.01**
Outer ring	213.9 $\pm$ 71.3	225.8 $\pm$ 66.7	208.5 $\pm$ 71.4	199.5 $\pm$ 76.1	**0.04**

Values printed in bold indicate statistical significance.

shows correlations between 2WAF and qAF in individual subfields of the ETDRS inner and outer rings.

DISCUSSION

Our data provide the first, to the best of our knowledge, detailed and quantitative assessment of metabolic autofluorescence imaging across the width of the high-risk macula lutea. We extended our previous findings of higher MPOD in AMD eyes than in healthy aged eyes by localizing them to mainly the ETDRS central subfield,[21,23] with the biggest contrasts between eAMD and iAMD eyes. The *z*-score maps of MPOD and qAF images in the macula lutea show MPOD increasing and qAF decreasing with AMD severity. MPOD meridian plots show asymmetries that do not appear in qAF meridian plots. Importantly, MPOD has annuli of signal consistent with variation in layer-to-layer content of xanthophyll carotenoids. Thus, the higher MPOD in AMD eyes is independent of changes in the RPE cell layer.

Variations in MPOD were fovea centered, with a low peak surrounded by annuli of lower and then higher intensities, like ripples heading outward from a stone landing in water. We believe that these details represent eccentricity-dependent differences in the thickness of xanthophyll-containing layers of the neurosensory retina,[31,84] shown schematically in Figure 1.[23,49] Incoming light passes through regions of varying layer thicknesses in the macula lutea that may collectively result in annular intensity variation around the central point. In contrast, the short-wavelength autofluorescence signal, measured as qAF, exhibited a broad and nearly uniform decrease in intensity with the presence and severity of AMD. These differences in MPOD and qAF topography potentially speak to different mechanistic influences. The MPOD distribution is clearly driven by variation in the structure of the overlying neurosensory retina. The broader distribution of lower qAF suggests other factors in the central outer retina. One possibility is microvascular involvement. For example, choriocapillaris dysfunction may impair bidirectional transport between the circulation and outer retina, inducing metabolic stress on the RPE and lowering qAF signals.[50–55]

Our analytic approach is informed by recent research strengthening the cellular basis of 2WAF imaging. Specifically, Müller glia are now recognized as major reservoirs of xanthophylls in the central retina. Loss of MP corresponded to loss of Müller glia markers in donor eyes with macular telangiectasia.[56–59] Müller glia markers and carotenoids were found in surgically excised lamellar hole epiretinal membranes,[60,61] and abundant Müller glia processes were found in foveal retinal layers where xanthophyll signals are strong.[62,63] High xanthophyll content in the Henle fiber layer has long attracted attention; however, the relative contribution to total xanthophyll by glia and neurons in the foveola (cones only) versus Henle fiber layer (cones and rods) remains to be determined. We proposed that the extension of xanthophyll-enriched membranes into the plexiform and nerve fiber layers of the macula lutea can account for the topographic distribution of AMD risk seen in population-based epidemiology.[15,18,21,64] This inference indicates that the xanthophyll bioavailability axis that supports high-acuity vision in primate retina is a critical and possibly driving component of the evolutionary biology of AMD.

Our topographical analysis showed higher MPOD in AMD than in normal eyes and a possibly different distribution anchored on the foveal center in eAMD and iAMD.

Mechanisms of intraretinal redistribution (e.g., within individual photoreceptors or Müller glia) are unknown at present. Our data can be compared to the results of Cozzi et al.,[22] who investigated retinal layer thicknesses and MPOD in healthy aged eyes and eyes with either macular drusen or subretinal drusenoid deposits (SDDs), using the indwelling SPECTRALIS software. These authors demonstrated that macular pigment optical volume (MPOD integrated over a specific area) was not significantly affected by the presence of either drusen or SDDs, consistent with our data indicating that AMD retinas are not lacking in xanthophyll carotenoids.[21,23] An alternative interpretation of lower 2WAF signal in the superior outer subfield of our iAMD eyes is that other structures are responsible. One candidate is SDDs, which are abundant in many of these same ALSTAR2 eyes in the same location.[65] However, SDDs are associated with an overall lower autofluorescence signal[66,67] due to thinner RPE cell bodies and rearrangement of apical processes containing melanosomes,[68] rather than absorption of light by the deposits themselves.

Our data pertain to a long-recognized paradox regarding visualizable aspects of macular physiology that impact AMD progression.[69] MP was considered protective, yet topographically tracked the distribution of AMD pathology identified in population-based epidemiology (i.e., high in the central subfield).[70] In contrast, autofluorescence signal sources in RPE were considered deleterious yet did not show this parallel. The paradox may be resolved by a well-supported multidisciplinary hypothesis equating the macula lutea and the 3-mm-diameter high-risk area, partly due to the lifelong delivery of dietary xanthophylls, as follows. MP is detectable chromatographically in RPE, possibly a transfer point between circulation and neurosensory retina.[71,72] Molecular mechanisms of selective xanthophyll uptake from the circulation and stabilization in the macula lutea (vs. extramacular retina) are actively being investigated and include the high-density lipoprotein (HDL) receptor SCARB1, among other proteins.[73–81] We proposed that RPE takes up xanthophylls on plasma lipoproteins and releases unneeded lipids in lipoprotein particles of its own.[21,64] Drusen form because age-related changes in the choriocapillaris and Bruch's membrane block lipoproteins from entering circulation, under the macula lutea. In contrast, short-wavelength autofluorescence (captured here as qAF) is expected to track the degradative load on RPE represented by the photoreceptor-to-RPE ratio (Fig. 1).[24] This peaks narrowly at the all-cone central bouquet and broadly in the ring of high rod density at 4- to 5-mm eccentricity, with a nadir just inside the rod-free zone.[24,82] This distribution is unrelated to that of AMD risk, at the current level of spatial resolution. Magnified qAF in the central 3-mm disk (Supplementary Fig. S1) possibly provides a glimpse of the central bouquet peak.

Our analysis is timely given a recent reanalysis of color fundus photographs from the AREDS2 trial potentially expanding the use of oral lutein and zeaxanthin supplementation. In brief, Keenan et al.[7] applied contemporary image analytic approaches to the original trial randomization and found that supplementation slows the expansion of pre-existing atrophy, especially toward the fovea. This effect was attributed to a possible enhancement of the naturally occurring phenomenon of foveal sparing in atrophy.[83–85] A protective effect also occurred in the AREDS trial, which did not test xanthophylls.[86] We focused on MP because of the strong cellular basis involving foveal neurons

and glia (see above), compared to a less well-specified site of action of other trialed antioxidants.[87] The AREDS2 trial hypothesized that MP improves retinal membrane stability, filters short-wavelength light, and maintains intra- and extracellular redox balance, among other mechanisms.[88–90] No specific AMD pathology was mentioned. Since the trials, much evidence now supports a progression sequence driven by extracellular deposits with Müller glia reactivity and persistence in atrophy.[19,64,91–93] To maximize the clinical and public health impact of valuable trial data, more studies using 2WAF technology and incorporating comprehensive models of AMD pathophysiology, like ALSTAR2, are needed.

Our data showing imaging correlates of foveal cell populations suggest future considerations for autofluorescence imaging technologies. 2WAF integrated over the central 3-mm disks remains informative for questions such as the effect of supplementation or dietary regimens and genetic underpinnings of xanthophyll bioavailability.[78,94] However, details of foveal anatomy that may confer risk for disease onset[95] will also require accurate layer-by-layer assignment of distinct metabolic signals. 2WAF will be most instructive when three-dimensional information from OCT is integrated into their interpretation. This includes conventional spectral domain OCT[41] and new visible light OCT approaches designed for xanthophyll localization.[96] In addition to monitoring outcomes of interventional studies, 2WAF may be a useful indicator of the many diverse yet partly unknown services that foveal Müller glia provide for cone-mediated vision.

Strengths of our study include a prospectively acquired dataset of 384 pseudophakic eyes stratified by a standard staging system and analyzed by recently introduced *z*-score maps to incorporate foveal variability. Because the underlying hypothesis of ALSTAR2 incorporates specific retinal cells, we used analytic approaches previously applied to anatomical studies of the neurosensory retina (i.e., maps and plots along the cardinal meridians). Pseudophakia avoids the influence of the natural lens on RPE autofluorescence signal. All custom software is publicly available for reproducing our results. Limitations of our study include the unequal balance of disease groups and lack of a personalized correction for natural lens autofluorescence[26] that could allow for a larger sample by including phakic eyes. By using disease stages determined by a classification system based on color fundus photography, our approach did not investigate specific AMD-related structural changes, which is a focus of future research.

In conclusion, we provide the first, to the best of our knowledge, detailed and quantitative assessment of metabolic maging across the width of the high-risk macula lutea, using current imaging technology. We expanded previous findings of increased MPOD in AMD compared to healthy aged eyes[21] by localizing them predominantly to the ETDRS central subfield. Although 2WAF imaging of MPOD utilizes RPE autofluorescence, 2WAF and qAF differ in eccentricity dependencies and variability statistics due to distinct cell populations. Incorporating variability is required for metabolic imaging of the high-risk region for AMD onset and progression, of importance for discerning influences that correspond with inheritance and genetic variation. Ongoing ALSTAR2 studies will investigate both 2WAF and qAF longitudinally for prognostic value and in relation to visual function.

References

1. Lim L, Mitchell P, Seddon JM, Holz FG, Wong TY. Age-related macular degeneration. *Lancet*. 2012;372:1835–1845.

2. Heier JS, Lad EM, Holz FG, et al. Pegcetacoplan for the treatment of geographic atrophy secondary to age-related macular degeneration (OAKS and DERBY): two multicentre, randomised, double-masked, sham-controlled, phase 3 trials. *Lancet*. 2023;402:1434–1448.

3. Khanani AM, Patel SS, Staurenghi G, et al. Efficacy and safety of avacincaptad pegol in patients with geographic atrophy (GATHER2): 12-month results from a randomised, double-masked, phase 3 trial. *Lancet*. 2023;402:1449–1458.

4. CATT Research Group. Ranibizumab and bevacizumab for neovascular age-related macular degeneration. *N Engl J Med*. 2011;364:1897–1908.

5. Age Related Eye Disease Study 2 (AREDS2) Research Group. Lutein + zeaxanthin and omega-3 fatty acids for age-related macular degeneration. *JAMA*. 2013;309:2005.

6. Chew EY, Clemons TE, Agrón E, et al. Long-term outcomes of adding lutein/zeaxanthin and *ω*-3 fatty acids to the AREDS supplements on age-related macular degeneration progression. *JAMA Ophthalmol*. 2022;140:692.

7. Keenan TDL, Agrón E, Keane PA, Domalpally A, Chew EY. Oral antioxidant and lutein/zeaxanthin supplements slow geographic atrophy progression to the fovea in age-related macular degeneration. *Ophthalmology*. 2025;132:14–29.

8. Morand-Laffargue L, Hirschberg J, Halimi C, Desmarchelier C, Borel P. The zeaxanthin present in a tomato line rich in this carotenoid is as bioavailable as that present in the food sources richest in this xanthophyll. *Food Res Int*. 2023;168:112751.

9. Böhm V, Lietz G, Olmedilla-Alonso B, et al. From carotenoid intake to carotenoid blood and tissue concentrations - implications for dietary intake recommendations. *Nutr Rev*. 2021;79:544–573.

10. Bohn T, Desmarchelier C, Dragsted LO, et al. Host-related factors explaining interindividual variability of carotenoid bioavailability and tissue concentrations in humans. *Mol Nutr Food Res*. 2017;61:1600685.

11. Koo E, Neuringer M, Sangiovanni JP. Macular xanthophylls, lipoprotein-related genes, and age-related macular degeneration. *Am J Clin Nutr*. 2014;100:336S–346S.

12. Green-Gomez M, Bernstein PS, Curcio CA, Moran R, Roche W, Nolan JM. Standardizing the assessment of macular pigment using a dual-wavelength autofluorescence technique. *Transl Vis Sci Technol*. 2019;8:41.

Investigative Ophthalmology & Visual Science

13. Conrady CD, Bell JP, Besch BM, et al. Correlations between macular, skin, and serum carotenoids. *Invest Ophthalmol Vis Sci*. 2017;58:3616–3627.

14. Wooten BR, Hammond BR, Jr. Spectral absorbance and spatial distribution of macular pigment using heterochromatic flicker photometry. *Optom Vis Sci*. 2005;82:378–386.

15. Curcio CA, Kar D, Owsley C, Sloan KR, Ach T. Age-related macular degeneration, a mathematically tractable disease. *Invest Ophthalmol Vis Sci*. 2024;65:4.

16. Domalpally A, Xing B, Pak JW, et al. Extramacular drusen and progression of age-related macular degeneration: age related eye disease study 2 report 30. *Ophthalmol Retina*. 2023;7:111–117.

17. Froines CP, Pak JW, Agrón E, et al. Longitudinal assessment of age-related macular degeneration using ultrawidefield imaging: the optos peripheral retina followup study [published online ahead of print November 30, 2024]. *Ophthalmology*, https://doi.org/10.1016/j.ophtha.2024.11.024.

18. Pollreisz A, Reiter GS, Bogunovic H, et al. Topographic distribution and progression of soft drusen volume in age-related macular degeneration implicate neurobiology of fovea. *Invest Ophthalmol Vis Sci*. 2021;62:26.

19. Curcio CA, McGwin G, Sadda SR, et al. Functionally validated imaging endpoints in the Alabama Study on Early Age-Related Macular Degeneration 2 (ALSTAR2): design and methods. *BMC Ophthalmol*. 2020;20:196.

20. Owsley C, Swain TA, McGwin G, Jr, Clark ME, Kar D, Curcio CA. Biologically guided optimization of test target location for rod-mediated dark adaptation in age-related macular degeneration: alabama study on early age-related macular degeneration 2 baseline. *Ophthalmol Sci*. 2023;3:100274.

21. McGwin G, Kar D, Berlin A, et al. Macular and Plasma xanthophylls are higher in age-related macular degeneration than in normal aging. *Ophthalmol Sci*. 2023;3:100263.

22. Cozzi M, Casaluci M, Ruggi G, et al. In vivo correlation between macular pigment optical volume and retinal layers thickness. *Invest Ophthalmol Vis Sci*. 2024;65:23.

23. Kar D, Clark ME, Swain TA, et al. Local abundance of macular xanthophyll pigment is associated with rod- and cone-mediated vision in aging and age-related macular degeneration. *Invest Ophthalmol Vis Sci*. 2020;61:46.

24. Berlin A, Fischer NA, Clark ME, et al. Quantitative autofluorescence at AMD's beginnings highlights retinal topography and grading system differences: ALSTAR2 baseline [published online ahead of print April 24, 2024]. *Ophthalmologica*, https://doi.org/10.1159/000538696.

25. Obana A, Gohto Y, Sasano H, et al. Grade of cataract and its influence on measurement of macular pigment optical density using autofluorescence imaging. *Invest Ophthalmol Vis Sci*. 2018;59:3011–3019.

26. von der Emde L, Rennen GC, Vaisband M, et al. Personalized lens correction improves quantitative fundus autofluorescence analysis. *Invest Ophthalmol Vis Sci*. 2024;65:13.

27. Reiter GS, Schwarzenbacher L, Schartmüller D, et al. Influence of lens opacities and cataract severity on quantitative fundus autofluorescence as a secondary outcome of a randomized clinical trial. *Sci Rep*. 2021;11:12685.

28. Davis MD, Gangnon RE, Hubbard B, et al. The Age-Related Eye Disease Study severity scale for age-related macular degeneration. *Arch Ophthalmol*. 2005;123:1598–1599.

29. Chew EY, Peto T, Clemons TE, et al. Macular telangiectasia type 2: a classification system using MultiModal Imaging MacTel Project Report Number 10. *Ophthalmol Sci*. 2023;3:100261.

30. Echols BS, Clark ME, Swain TA, et al. Hyperreflective foci and specks are associated with delayed rod-mediated dark adaptation in nonneovascular age-related macular degeneration. *Ophthalmol Retina*. 2020;4:1059–1068.

31. You QS, Bartsch D-UG, Espina M, et al. Reproducibility of macular pigment optical density measurement by two-wavelength autofluorescence in a clinical setting. *Retina*. 2016;36:1381–1387.

32. Greenberg JP, Duncker T, Woods RL, Smith RT, Sparrow JR, Delori FC. Quantitative fundus autofluorescence in healthy eyes. *Invest Ophthalmol Vis Sci*. 2013;54:5684–5693.

33. Delori F, Greenberg JP, Woods RL, et al. Quantitative measurements of autofluorescence with the scanning laser ophthalmoscope. *Invest Ophthalmol Vis Sci*. 2011;52:9379–9390.

34. Theelen T. Scanning laser imaging of the retina. Basic concepts and clinical applications. Available at: https://www.researchgate.net/publication/232768942_Scanning_Laser_Imaging_of_the_Retina_-_Basic_Concepts_and_Clinical_Appplications. Accessed March 14, 2025.

35. von der Emde L, Guymer RH, Pfau M, et al. Natural history of quantitative autofluorescence in intermediate age-related macular degeneration. *Retina*. 2021;41:694–700.

36. Reiter GS, Told R, Baratsits M, et al. Repeatability and reliability of quantitative fundus autofluorescence imaging in patients with early and intermediate age-related macular degeneration. *Acta Ophthalmol*. 2019;97:e526–e532.

37. Sparrow JR, Blonska A, Flynn E, et al. Quantitative fundus autofluorescence in mice: correlation with HPLC quantitation of RPE lipofuscin and measurement of retina outer nuclear layer thickness. *Invest Ophthalmol Vis Sci*. 2013;54:2812–2820.

38. von der Emde L, Mallwitz M, Vaisband M, et al. Retest variability and patient reliability indices of quantitative fundus autofluorescence in age-related macular degeneration: a MACUSTAR study report. *Sci Rep*. 2023;13:17417.

39. Schindelin J, Arganda-Carreras I, Frise E, et al. Fiji: an open-source platform for biological-image analysis. *Nat Methods*. 2012;9:676–682.

40. Sauer L, Andersen KM, Li B, Gensure RH, Hammer M, Bernstein PS. Fluorescence lifetime imaging ophthalmoscopy (FLIO) of macular pigment. *Invest Ophthalmol Vis Sci*. 2018;59:3094–3103.

41. Obana A, Gohto Y, Sasano H, et al. Spatial distribution of macular pigment estimated by autofluorescence imaging in elderly Japanese individuals. *Jpn J Ophthalmol*. 2020;64:160–170.

42. Kleefeldt N, Bermond K, Tarau IS, et al. Quantitative fundus autofluorescence: advanced analysis tools. *Transl Vis Sci Technol*. 2020;9:1–11.

43. Berlin A, Clark ME, Swain TA, et al. Impact of the aging lens and posterior capsular opacification on quantitative autofluorescence imaging in age-related macular degeneration. *Transl Vis Sci Technol*. 2022;11:23.

44. Vajzovic L, Hendrickson AE, O'Connell RV, et al. Maturation of the human fovea: correlation of spectral-domain optical coherence tomography findings with histology. *Am J Ophthalmol*. 2012;154:779–789.e2.

45. Goerdt L, Swain TA, Kar D, et al. Band visibility in high-resolution optical coherence tomography assessed with a custom review tool and updated, histology-derived nomenclature. *Transl Vis Sci Technol*. 2024;13:19.

46. Bringmann A, Syrbe S, Gorner K, et al. The primate fovea: structure, function and development. *Prog Retin Eye Res*. 2018;66:49–84.

47. Wickham H. *ggplot2: elegant graphics for data analysis*: New York: Springer-Verlag; 2016.

48. R Project for Statistical Computing. *R: A Language and Environment for Statistical Computing*. Vienna, Austria: R Foundation for Statistical Computing; 2022.

49. Li B, Vachali P, Chang FY, et al. HDL is the primary transporter for carotenoids from liver to retinal pigment epithe-

Investigative Ophthalmology & Visual Science

lium in transgenic ApoA-I(−/−)/Bco2(−/−) mice. *Arch Biochem Biophys*. 2022;716:109111.

50. Ramrattan RS, van der Schaft TL, Mooy CM, de Bruijn WC, Mulder PGH, de Jong PT. Morphometric analysis of Bruch's membrane, the choriocapillaris, and the choroid in aging. *Invest Ophthalmol Vis Sci*. 1994;35:2857–2864.

51. Mullins RF, Schoo DP, Sohn EH, et al. The membrane attack complex in aging human choriocapillaris. *Am J Pathol*. 2014;184:3142–3153.

52. Zheng F, Zhang Q, Shi Y, et al. Age-dependent changes in the macular choriocapillaris of normal eyes imaged with swept-source optical coherence tomography angiography. *Am J Ophthalmol*. 2019;200:110–122.

53. Kar D, Corradetti G, Swain TA, et al. Choriocapillaris impairment is associated with delayed rod-mediated dark adaptation in age-related macular degeneration. *Invest Ophthalmol Vis Sci*. 2023;64:41.

54. Kar D, Amjad M, Corradetti G, et al. Choriocapillaris impairment, visual function, and distance to fovea in aging and age-related macular degeneration: ALSTAR2 baseline. *Invest Ophthalmol Vis Sci*. 2024;65:40.

55. Nassisi M, Tepelus T, Corradetti G, Sadda SR. Relationship between choriocapillaris flow and scotopic microperimetry in early and intermediate age-related macular degeneration. *Am J Ophthalmol*. 2021;222:302–309.

56. Powner MB, Gillies MC, Tretiach M, et al. Perifoveal Müller cell depletion in a case of macular telangiectasia type 2. *Ophthalmology*. 2010;117:2407–2416.

57. Powner MB, Gillies MC, Zhu M, Vevis K, Hunyor AP, Fruttiger M. Loss of Müller's cells and photoreceptors in macular telangiectasia type 2. *Ophthalmology*. 2013;120:2344–2352.

58. Zeimer MB, Krömer I, Spital G, Lommatzsch A, Pauleikhoff D. Macular telangiectasia: patterns of distribution of macular pigment and response to supplementation. *Retina*. 2010;30:1282–1293.

59. Zeimer MB, Padge B, Heimes B, Pauleikhoff D. Idiopathic macular telangiectasia type 2: distribution of macular pigment and functional investigations. *Retina*. 2010;30:586–595.

60. Pang CE, Maberley DA, Freund KB, et al. Lamellar hole-associated epiretinal proliferation: a clinicopathologic correlation. *Retina*. 2016;36:1408–1412.

61. Pang CE, Spaide RF, Freund KB. Epiretinal proliferation seen in association with lamellar macular holes: a distinct clinical entity. *Retina*. 2014;34:1513–1523.

62. Kar D, Singireddy R, Kim YJ, et al. Unusual morphology of foveal Müller glia in an adult human born pre-term. *Front Cell Neurosci*. 2024;18:1409405.

63. Ahmad KM, Klug K, Herr S, Sterling P, Schein S. Cell density ratios in a foveal patch in macaque retina. *Vis Neurosci*. 2003;20:189–209.

64. Curcio CA. Antecedents of soft drusen, the specific deposits of age-related macular degeneration, in the biology of human macula. *Invest Ophthalmol Vis Sci*. 2018;59:AMD182–AMD194.

65. Goerdt L, Amjad M, Swain TA, et al. Extent and topography of subretinal drusenoid deposits associate with rod-mediated vision in aging and AMD: ALSTAR2 baseline. *Invest Ophthalmol Vis Sci*. 2024;65:25.

66. Smith RT, Chan JK, Busuoic M, Sivagnanavel V, Bird AC, Chong NV. Autofluorescence characteristics of early, atrophic, and high-risk fellow eyes in age-related macular degeneration. *Invest Ophthalmol Vis Sci*. 2006;47:5495–5504.

67. Gliem M, Müller PL, Finger RP, McGuinness MB, Holz FG, Issa PC. Quantitative fundus autofluorescence in early and intermediate age-related macular degeneration. *JAMA Ophthalmol*. 2016;134:817–824.

68. Anderson DMG, Kotnala A, Migas LG, et al. Lysolipids are prominent in subretinal drusenoid deposits, a high-risk phenotype in age-related macular degeneration. *Front Ophthalmol (Lausanne)*. 2023;3:1258734.

69. Jackson GR, Owsley C, Curcio CA. Photoreceptor degeneration and dysfunction in aging and age-related maculopathy. *Ageing Res Rev*. 2002;1:381–396.

70. Snoddery DM. Evidence for protection against age-related macular degeneration by carotenoids and antioxidant vitamins. *Am J Clin Nutr*. 1995;62:1448s–1461s.

71. Li B, George EW, Rognon GT, et al. Imaging lutein and zeaxanthin in the human retina with confocal resonance Raman microscopy. *Proc Natl Acad Sci USA*. 2020;117:12352–12358.

72. Bernstein PS, Khachik F, Carvalho LS, Muir GJ, Zhao DY, Katz NB. Identification and quantitation of carotenoids and their metabolites in the tissues of the human eye. *Exp Eye Res*. 2001;72:215–223.

73. Li B, Vachali P, Frederick JM, Bernstein PS. Identification of StARD3 as a lutein-binding protein in the macula of the primate retina. *Biochemistry*. 2011;50:2541–2549.

74. Connor WE, Duell PB, Kean R, Wang Y. The prime role of HDL to transport lutein into the retina: evidence from HDL-deficient WHAM chicks having a mutant ABCA1 transporter. *Invest Ophthalmol Vis Sci*. 2007;48:4226–4231.

75. Li B, George EW, Vachali P, et al. Mechanism for the selective uptake of macular carotenoids mediated by the HDL cholesterol receptor SR-BI. *Exp Eye Res*. 2023;229:109429.

76. Bhosale P, Larson AJ, Frederick JM, Southwick K, Thulin CD, Bernstein PS. Identification and characterization of a pi isoform of glutathione S-transferase (GSTP1) as a zeaxanthin-binding protein in the macula of the human eye. *J Biol Chem*. 2004;279:49447–49454.

77. During A, Doraiswamy S, Harrison EH. Xanthophylls are preferentially taken up compared with β-carotene by retinal cells via a SRBI-dependent mechanism. *J Lipid Res*. 2008;49:1715–1724.

78. Meyers KJ, Johnson EJ, Bernstein PS, et al. Genetic determinants of macular pigments in women of the Carotenoids in Age-Related Eye Disease Study. *Invest Ophthalmol Vis Sci*. 2013;54:2333–2345.

79. Neale BM, Fagerness J, Reynolds R, et al. Genome-wide association study of advanced age-related macular degeneration identifies a role of the hepatic lipase gene (LIPC). *Proc Natl Acad Sci USA*. 2010;107:7395–7400.

80. SanGiovanni JP, Neuringer M. The putative role of lutein and zeaxanthin as protective agents against age-related macular degeneration: promise of molecular genetics for guiding mechanistic and translational research in the field. *Am J Clin Nutr*. 2012;96:1223S–1233S.

81. Li B, Chang FY, Wan Z, Giauque NA, Addo EK, Bernstein PS. Imaging macular carotenoids and their related proteins in the human retina with confocal resonance Raman and fluorescence microscopy. *Exp Eye Res*. 2024;247:110043.

82. Snoddery DM, Sandstorm MM, Leung I, Zucker CL, Neuringer M. Retinal pigment epithelial cell distribution in central retina of rhesus monkeys. *Invest Ophthalmol Vis Sci*. 2002;43:2815–2818.

83. Bax NM, Valkenburg D, Lambertus S, et al. Foveal sparing in central retinal dystrophies. *Invest Ophthalmol Vis Sci*. 2019;60:3456–3467.

84. Lindner M, Böker A, Mauschitz MM, et al. Directional kinetics of geographic atrophy progression in age-related macular degeneration with foveal sparing. *Ophthalmology*. 2015;122:1356–1365.

85. Lindner M, Pfau M, Czauderna J, et al. Determinants of reading performance in eyes with foveal-sparing geographic atrophy. *Ophthalmol Retina*. 2019;3:201–210.

86. Age-Related Eye Disease Study Research Group. The Age-Related Eye Disease Study (AREDS): design implications. AREDS report no. 1. *Control Clin Trials*. 1999;20:573–600.

87. Datta S, Cano M, Ebrahimi K, Wang L, Handa JT. The impact of oxidative stress and inflammation on RPE degeneration in non-neovascular AMD. *Prog Retin Eye Res*. 2017;60:201–218.

88. Stringham JM, Garcia PV, Smith PA, et al. Macular pigment and visual performance in low-light conditions. *Invest Ophthalmol Vis Sci*. 2015;56:2459–2468.

89. Bernstein PS, Li B, Vachali PP, et al. Lutein, zeaxanthin, and meso-zeaxanthin: the basic and clinical science underlying carotenoid-based nutritional interventions against ocular disease. *Prog Retin Eye Res*. 2016;50:34–66.

90. Krinsky NI, Landrum JT, Bone RA. Biologic mechanisms of the protective role of lutein and zeaxanthin in the eye. *Annu Rev Nutr*. 2003;23:171–201.

91. Curcio CA. Soft drusen in age-related macular degeneration: biology and targeting via the oil spill strategies. *Invest Ophthalmol Vis Sci*. 2018;59:AMD160–AMD181.

92. Sura AA, Chen L, Messinger JD, et al. Measuring the contributions of basal laminar deposit and Bruch's membrane in age-related macular degeneration. *Invest Ophthalmol Vis Sci*. 2020;61:19.

93. Chen L, Messinger JD, Ferrara D, Freund KB, Curcio CA. Stages of drusen-associated atrophy in age-related macular degeneration visible via histologically validated fundus autofluorescence. *Ophthalmol Retina*. 2021;5:730–742.

94. Meyers KJ, Mares JA, Igo RP, et al. Genetic evidence for role of carotenoids in age-related macular degeneration in the Carotenoids in Age-Related Eye Disease Study (CAREDS). *Invest Ophthalmol Vis Sci*. 2014;55:587–599.

95. Wagner-Schuman M, Dubis AM, Nordgren RN, et al. Race- and Sex-related differences in retinal thickness and foveal pit morphology. *Invest Ophthalmol Vis Sci*. 2011;52:625–634.

96. Gupta AK, Meng R, Modi YS, Srinivasan VJ. Imaging human macular pigments with visible light optical coherence tomography and superluminescent diodes. *Opt Lett*. 2023;48:4737–4740.

97. Snodderly DM, Auran JD, Delori FC. The macular pigment. II. Spatial distribution in primate retinas. *Invest Ophthalmol Vis Sci*. 1984;25:674–685.

98. Trieschmann M, Spital G, Lommatzsch A, et al. Macular pigment: quantitative analysis on autofluorescence images. *Graefes Arch Clin Exp Ophthalmol*. 2003;241:1006–1012.